

Self-hybridization within non-Hermitian localized plasmonic systems

Hugo Lourenço-Martins, Pabitra Das, Luiz H. G. Tizei, Raphaël Weil and Mathieu Kociak *

The orthogonal eigenmodes are well-defined solutions of Hermitian equations describing many physical situations from quantum mechanics to acoustics. However, a large variety of non-Hermitian problems, including gravitational waves close to black holes or leaky electromagnetic cavities, require the use of a bi-orthogonal eigenbasis with consequences challenging our physical understanding^{1–4}. The need to compensate for energy losses made the few successful attempts^{5–8} to experimentally probe non-Hermiticity extremely complicated. We overcome this problem by considering localized plasmonic systems. As the non-Hermiticity in these systems does not stem from temporal invariance breaking but from spatial symmetry breaking, its consequences can be observed more easily. We report on the theoretical and experimental evidence for non-Hermiticity-induced strong coupling between surface plasmon modes of different orders within silver nanodaggers. The symmetry conditions for triggering this counter-intuitive self-hybridization phenomenon are provided. Similar observable effects are expected to exist in any system exhibiting bi-orthogonal eigenmodes.

In any situation described by a Hermitian equation (such as mechanics, acoustics, quantum mechanics and electromagnetism), the usual approach in linear physics is to apply the concept of eigenmodes. Examples are endless: the vibrations of a guitar string are best understood as a superposition of the string eigenmodes and the properties of an atom can be simply deduced from its orbitals' properties. It is thus tempting to adapt this concept to systems in which eigenmodes are harder to define, namely for non-Hermitian systems.

One class of non-Hermitian systems consists of open systems that span a wide range of physical situations, from gravity waves close to black holes to lasers cavities or propagating surface plasmons^{9–12}. In those cases, quasi-normal modes (QNMs) are specially constructed so that time-reversal symmetry breaking does not prevent the establishment of a complete basis, especially when parity–time symmetry is preserved. Another class is represented by localized surface plasmons (LSPs). In this case, the structure of the constituting equation is non-symmetric.

In the two cases, a bi-orthogonal rather than orthogonal basis must be used. A full quantum theory of bi-orthogonal modes has been developed^{1,3}. Bi-orthogonality has a few famous and exciting consequences, including the existence of 'exceptional points' where both the energy and wavefunctions coalesce^{2,13–15}. Exceptional points are usually associated with the apparition of non-trivial physical effects, such as asymmetric mode switching¹⁴. Such effects have only very recently been studied experimentally^{5,7,8,16}

because manipulating QNMs in open systems requires to exactly balance dissipation^{2,17}. Surprisingly, using LSPs to explore non-Hermitian physics has not been reported, although dissipation balancing is not required in this case. Moreover, describing LSP physics with bi-orthogonal modes has mostly been seen as an extra mathematical annoyance¹⁸ that does not violate our common understanding.

Here, we show that non-Hermitian physics can be investigated theoretically and experimentally with LSPs. We show that both the surface plasmon equation's kernel symmetry and the overall system symmetry have to be tuned towards revealing bi-orthogonality signatures. As a direct and counter-intuitive consequence of non-Hermiticity, we predict and observe experimentally in the case of silver nanodaggers the coupling of two bi-orthogonal modes of different orders within a single plasmonic particle (self-hybridization). Defining the relevant free energy, we then draw an analogy between plasmons and other non-Hermitian systems. Given the easily tunable parameters, we conclude that LSPs constitute an excellent platform for probing non-Hermitian physics.

Within the quasi-static limit, it has been shown¹⁹ that the plasmon modes are bi-orthogonal solutions of a Fredholm non-Hermitian eigenvalue problem that reads:

$$\begin{aligned} F | \sigma_m \rangle &= \lambda_m | \sigma_m \rangle, \\ \langle \tau_m | F &= \lambda_m \langle \tau_m |, \\ F(\mathbf{r}, \mathbf{r}') &= -\frac{\mathbf{n}(\mathbf{r}) \cdot (\mathbf{r} - \mathbf{r}')}{|\mathbf{r} - \mathbf{r}'|^3} \text{ where } \mathbf{r}, \mathbf{r}' \in S \end{aligned} \quad (1)$$

where $\mathbf{n}(\mathbf{r})$ is the outgoing normal to surface S at \mathbf{r} , F is the normal derivative of the Coulomb kernel, the right eigenvectors $\{| \sigma_m \rangle\}$ can be identified as surface charge densities, the left eigenvectors $\{\langle \tau_m | \}$ are surface dipole densities projected along \mathbf{n} and the eigenvalues $\{\lambda_m\}$ are dimensionless quantities associated with each pair of left–right eigenvectors. Hence, in contrast to systems recently considered^{7,8,20–23}, non-Hermiticity arises from the non-symmetry of F , which is always real. Solutions of equation (1) can be computed with the boundary element method (BEM)^{18,24–27}. The integer m indexes the modes by increasing values of λ_m . In the following, for the sake of simplicity, we will indifferently discuss the geometrical eigenvalues $\{\lambda_m\}$, which are real¹⁹ or the plasmon eigenenergies $\{\omega_m\}$ assuming a one-to-one correspondence between the two spaces $\{\lambda_m\} \leftrightarrow \{\omega_m\}$.

There are fundamentally two types of symmetry involved in a plasmonic eigenproblem. The first one is the kernel symmetry (F -symmetry) that controls the structure of the vector space

Laboratoire de Physique des Solides, Univ. Paris-Sud, CNRS UMR 8502, Orsay, France. H. Lourenço-Martins and P. Das contributed equally to this work.

*e-mail: mathieu.kociak@u-psud.fr

solution and thus the (bi-)orthogonality of the plasmon modes. It can be shown that F -symmetric surface configurations ($F^T = F$) satisfy (see Supplementary Information):

$$(\mathbf{n}(\mathbf{r}) + \mathbf{n}(\mathbf{r}')) \cdot (\mathbf{r} - \mathbf{r}') = 0 \quad (2)$$

where $\mathbf{n}(\mathbf{r})$ is the normal vector in \mathbf{r} . The second is the surface symmetry (S -symmetry); that is, the invariance of the surface charge or dipole distributions under any geometrical transformation, which may lead to additional properties of the plasmons. As a practical example, in Fig. 1a, we present σ and τ corresponding to the first two eigenmodes of an F -symmetric surface (sphere) and an F -asymmetric surface (torus). For the sphere, the solutions are orthogonal and thus the left and right eigenvectors are identical while, in the case of the torus, the solutions are bi-orthogonal and the corresponding left and right eigenvectors are strikingly different.

In Fig. 1b, we show four F -symmetric configurations A–D. One can immediately deduce that a sphere (C), a cylinder (A, B and C), a cuboid²⁸ (A, B and D) or a disc (C and D) are F -symmetric. Similarly, in Fig. 1c, the cross and the dagger (see inset) are F -asymmetric.

Counter-intuitively, when a surface is F -asymmetric, two right (or left) eigenvectors of different orders may have a non-zero spatial overlap. The consequent interaction should increase with increasing overlap; therefore, one could formulate the following ansatz:

$$\Omega_{m,n} \propto T_{m,n} \quad (3)$$

where $\Omega_{n,m}$ is the so-called classical Rabi energy of the two interacting modes n and m . The overlap matrix $T_{m,n} = \langle \tau_m | \tau_n \rangle \langle \sigma_m | \sigma_n \rangle + \langle \sigma_m | \sigma_n \rangle \langle \tau_m | \tau_n \rangle$ thus constitutes a fundamental quantity to consider in the study of bi-orthogonal systems.

We must emphasize that the resulting self-hybridization mediated by the eigencharges coupling we consider here is fundamentally different from the coupling in orthogonal systems mediated by the fields. In Fig. 1d, we plot the absolute value of $T_{m,n}$ between the first ten eigenmodes of a sphere, a torus, a cross and a dagger. Indeed, all of the eigenvectors are determined up to an $e^{i\pi}$ phase. Consequently $T_{m,n}$ can indifferently take two values $\pm T_{m,n}$. To remove this uncertainty and to increase the dynamics of the colour scale, we plot the absolute value of the overlap matrix. With the sphere being F -symmetric, $T_{m,n} = \delta_{m,n}$ as expected. The torus is F -asymmetric but $T_{m,n}$ is diagonal as a consequence of its strong S -symmetry (rotational invariance). Consequently, although F -asymmetric, the torus behaves essentially like an orthogonal system, with the only difference being the absence of normalization of the elements on the diagonal. Cross and dagger are two F -asymmetric structures that display weaker S -symmetry than the torus (see inset Fig. 1c). The cross is still centro-symmetric, which imposes a null overlap between modes of different parity; that is, $\langle \sigma_m | \sigma_n \rangle = \langle \tau_m | \tau_n \rangle = 0$ if $n + m$ is odd, resulting in the appearance of a checkerboard-like matrix. A comprehensive experimental and numerical study of the plasmonic cross system away from the hybridization point is developed in ref.²⁹. By shifting one arm of the cross, we break the centro-symmetry and the last relation does not hold anymore. Consequently, the dagger overlap matrix has most of its off-diagonal elements with non-null values (see Supplementary Information). Therefore, when the surface is F -asymmetric, the S -symmetry is the parameter controlling the overlap between modes of different orders.

For the sake of the demonstration, we first consider $400 \text{ nm} \times L$ silver crosses with a $40 \times 40 \text{ nm}$ square cross-section. The length L , which will be shown to be the relevant detuning parameter, is varied from 75 nm to 170 nm . The effect of the variation of L on the eigenquantities can be modelled using first-order perturbation theory. This approximation is formally derived for bi-orthogonal systems in ref.³ and has been introduced for the BEM³⁰. Within this approximation, one can treat a small geometrical deformation

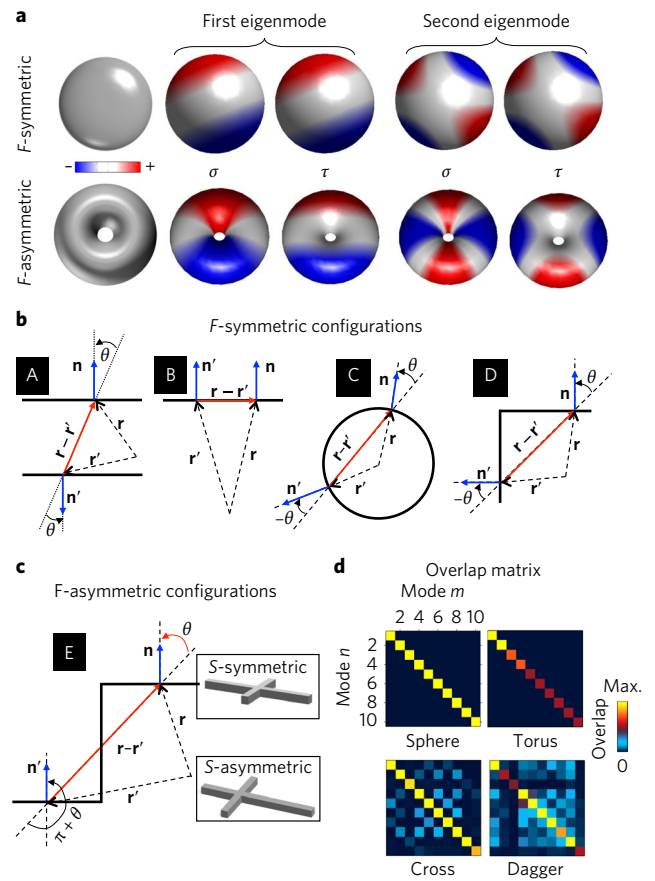


Fig. 1 | Symmetry-driven bi-orthogonality in LSP systems. **a**, The first two left and right eigenvectors of F -symmetric (sphere) and F -asymmetric (torus) surfaces. **b**, Geometrical configurations of two normal vectors located on the surface leading to a symmetric contribution to the kernel. **c**, Example of an asymmetric configuration corresponding, for example, to a cross or a dagger particle. **d**, Overlap matrix between the first ten eigenmodes of a sphere, a torus, a cross and a dagger. Calculations have been performed according with the BEM method (see Methods and Supplementary Information).

of the particle as a perturbation of the kernel $F \rightarrow F + \delta F$, leading to a shift in the eigenvalues $\lambda_m^{(0)} \rightarrow \lambda_m^{(0)} + \lambda_m^{(1)}$ but not to modification of the eigenvectors. This was elegantly used to analyse mode evolution when morphing a nanotriangle into a nanodisc²⁸. Within the perturbation theory, when two modes spectrally overlap, one has to take into account the possible hybridization between them³¹ by diagonalizing the typical Rabi-like matrix:

$$M = \begin{pmatrix} \lambda_m^{(0)} + \lambda_m^{(1)} & C_{m,n} \\ C_{n,m} & \lambda_n^{(0)} + \lambda_n^{(1)} \end{pmatrix} \quad (4)$$

Using the convention of refs^{32–35}, we call diabatic the eigenvectors of the unperturbed basis $\{\sigma_m^{(0)}, \tau_m^{(0)}\}$ in which M is expressed in equation (4), and adiabatic the eigenvectors of the hybridized basis $\{\sigma_{m,n}^{\pm}, \tau_{m,n}^{\pm}\}$ in which M is diagonal. Equation (4) is similar to the linear combination of atomic orbital theory³¹ that describes the hybridization between orbitals belonging to different systems. Therefore, it can efficiently model dimer-like coupling where the two hybridized modes belong to two different and independent surfaces that can be either two monomers³⁶ or two independent sub-surfaces of a large monomer²⁸. In contrast, the self-hybridization process we introduce here is counter-intuitive, as it takes

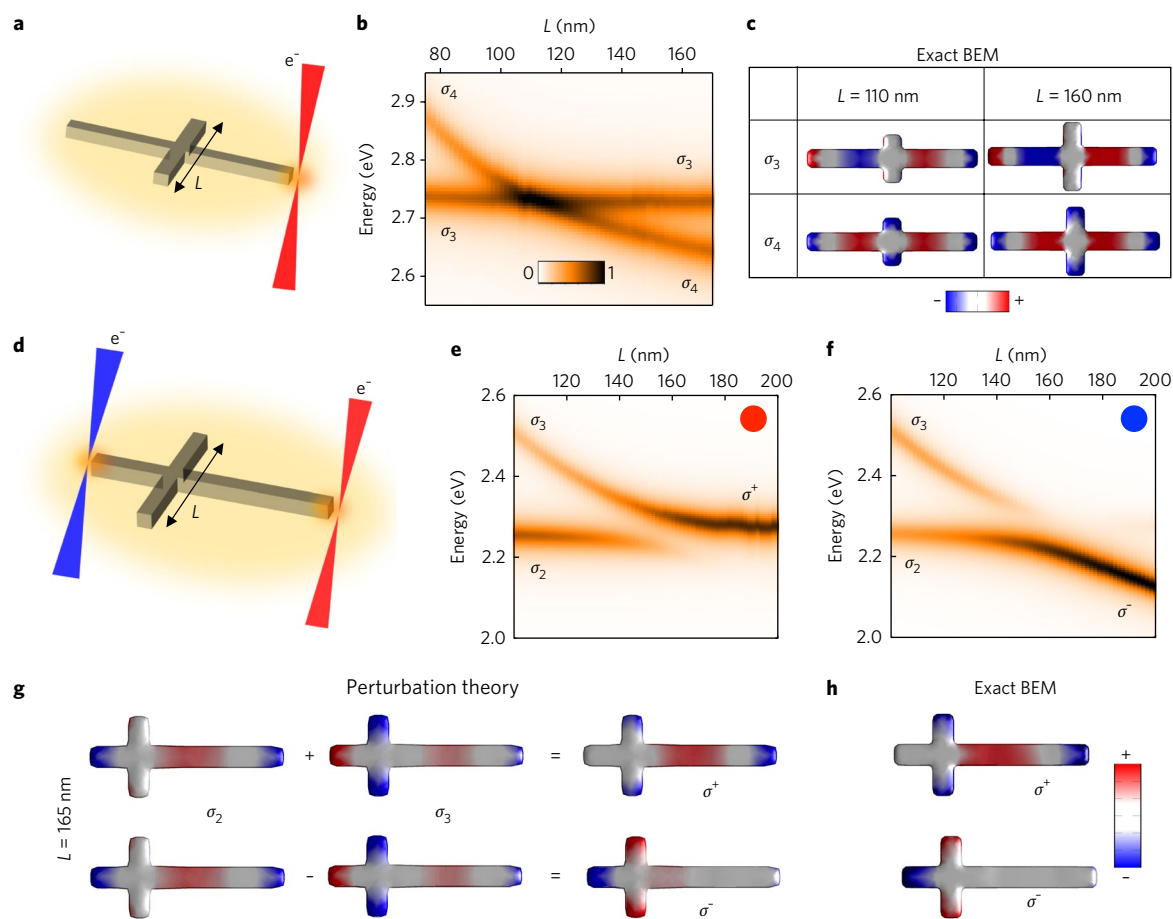


Fig. 2 | Self-hybridization principle. **a**, Schematic representation of an EELS experiment on a cross. **b**, Simulated EEL spectra taken at the position of the electron beam indicated in **a** as a function of L . **c**, Simulated right eigenvectors corresponding to modes 3 and 4 at ($L = 110$ nm) and after ($L = 160$ nm) the crossing point. **d**, Schematic representation of an EELS experiment on the dagger. **e**, Simulated EEL spectra taken at the red position of the electron beam indicated in **d** as a function of L . **f**, Simulated EEL spectra taken at the blue position of the electron beam indicated in **d** as a function of L . **g**, Hybridized eigenvectors calculated at the anti-crossing point using first-order perturbation theory. **h**, Hybridized eigenvectors calculated at the anti-crossing point using the exact BEM.

place within a single surface and would be comparable, for example, to the hybridization between s and p orbitals within a single atom, and not between two atoms.

When the two modes are perfectly degenerated ($\lambda_m = \lambda_n$), one can show that the mixing term reads (see Supplementary Information):

$$C_{n,m} = \langle \tau_n^{(0)} | \delta F | \sigma_m^{(0)} \rangle = \lambda_m^{(1)} T_{n,m} \quad (5)$$

Thus, one can immediately see that self-hybridization is possible only when $T_{n,m} \neq 0$; that is, when the system is bi-orthogonal. In other words, the surface defining the diabatic modes needs to be F -asymmetric while the F -symmetry of the perturbative kernel δF can be arbitrary. The mixing term $C_{n,m}$ can be mapped in energy space to the classical Rabi energy $\Omega_{n,m}$ which justifies equation (3). Measuring the energy splitting at maximum coupling gives $\Omega_{n,m}$ and therefore a measurement of the degree of bi-orthogonality of a system.

We also note that it has been proposed³⁵ phenomenologically that harmonic plasmonic modes within single nanorods could hybridize. However, the one-dimensional confinement along the long axis of the ellipsis induces a hierarchical (harmonic) quantification of surface plasmon energies that prevents modes of different orders from having degenerate eigenvalues even for F -asymmetric nanorods, probably explaining the weakness of the observed effect.

Electron energy-loss spectroscopy (EELS) is a spectroscopy ideally suited for nanoplasmonics³⁷ (see Methods). In Fig. 2a,b, we calculate EELS spectra of a function of L for a nanocross. When L is small, the cross eigenmodes have the same spatial profile as the well-known rod eigenmodes³⁵, with eigenvectors $|\sigma_n\rangle$ displaying periodic profiles with n nodes (Fig. 2c). With increasing L , the odd modes, having no charge at the centre, remain almost unchanged while the even modes redshift. Consequently, for particular values of L , modes of different parity can spectrally overlap, justifying the use of L as a detuning parameter. As shown in Fig. 2b, when $L = 110$ nm, modes 3 and 4 spectrally overlap. However, although the cross is F -asymmetric, no sign of self-hybridization appears as the corresponding eigenvectors keep the same spatial profile at and after the crossing point (see Fig. 2c). To enable self-hybridization, the (S -)centro-symmetry of the cross needs to be broken, for example by producing a dagger by shifting an arm (Fig. 2d). The position of the small arm of the dagger is chosen to correspond to a maximum of mode 3 and a node of mode 2, so that the energy of the mode 3 (respectively 2) should largely disperse (non-disperse) with L and make energy degeneracy possible. In Fig. 2e,f, we calculate the EELS spectra as a function of L at two positions of the beam where modes 2 and 3 are efficiently detected. The spectra display a strong anti-crossing behaviour. To validate our earlier interpretation, we calculate the adiabatic (hybridized) modes σ^\pm both using the first-order perturbation theory and the exact BEM in Fig. 2g,h at the

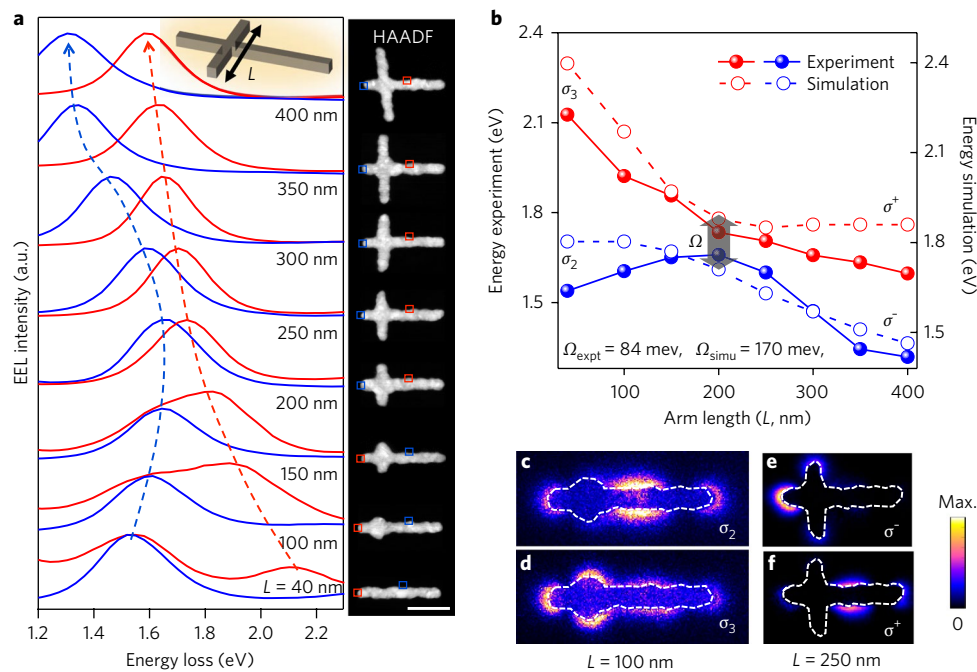


Fig. 3 | Experimental observation of self-hybridization in nanodaggers. **a**, Experimental EELS spectra for different arm lengths zoomed on the mode 2 and 3 energy regions. (a.u., arbitrary units.) EELS spectra have been extracted from full spectral images, deconvoluted following prescriptions in refs^{37,44} and summed on the regions of interest indicated on the right high-angle annular dark-field (HAADF) images by the corresponding colours (see Methods). Scale bar, 200 nm. The regions have been chosen for isolating as much as possible the spectral signature of each mode. Note the colouring swap due to symmetry exchange at the anti-crossing point. Corresponding raw data are presented in the Supplementary Information. **b**, Experimental and simulated energy of the modes in **a** as a function of the arm length L . Experimental energies have been deduced by Gaussian fit (see Methods). Note the shift of the energy axis between experiment and theory related to the absence of substrate in the simulations²⁹. **c,d**, EELS filtered maps measured at energies corresponding to an uncoupled case for $L=100$ nm. **e,f**, EELS fitted maps for the coupled case at $L=250$ nm. A full set of EELS maps is given in the Supplementary Information.

crossing point ($L=165$ nm) where the adiabatic modes are known to be equal mixtures of diabatic modes $\sigma^\pm = \sigma_2 \pm \sigma_3$. The two results are in remarkably good agreement, proving that the perturbation theory gives a realistic picture of the self-hybridization physics.

One can highlight the exotic profile of the hybrid modes. In particular, the mode σ^- strongly confines charges at one tip, leading to a so-called hotspot configuration that is of particular interest in a wide range of applications. Self-hybridization thus constitutes a very attractive procedure for designing specific plasmonic states.

Ω_{nm} is predicted to be sufficiently large to be measured. We therefore lithographed a series of silver daggers with increasing L and measured the energy and spatial distribution of modes 2 and 3 using spatially resolved EELS³⁷ (see Methods).

We report in Fig. 3a the characteristic spectra extracted from spectral images (see Methods) acquired on a series of daggers with varying arm length L . Figure 3b summarizes the behaviour of the energies of the plasmon peak maxima as a function of L . One can see that we reproduce the anti-crossing behaviour calculated in Fig. 2. The lower (σ^-) and upper (σ^+) branches are separated by a coupling constant $\Omega_{\text{exp}} \approx 84$ meV, a remarkably high value considering that the studied structures are lithographed polycrystalline particles. In Fig. 3c, we report the EELS maps measured at the resonance energies for two different values of L (see Methods). When $L=100$ nm, the two modes display the spatial signature of the diabatic modes σ_2 and σ_3 , showing that the two plasmons modes are not coupled. At $L=250$ nm, the coupling regime is clearly established as the two adiabatic plasmon modes display the characteristic spatial distributions expected from Fig. 2h. In the Supplementary Information, we also present the full set of EELS maps together with the simulated charge densities, showing the symmetry exchange expected for self-hybridization away from the anti-crossing point.

We will conclude by connecting the present work to analogous effects encountered in other non-Hermitian domains of physics. Non-Hermiticity has been observed in a wide range of systems (for example, leaky electromagnetic cavities²¹, acoustic cavities⁸ or electronic resonators⁵, to name a few). Moreover, non-Hermitian effects have also been considered in (propagating) plasmonic systems^{12,16}. In these systems, non-Hermiticity arises from broken time-reversal symmetry. The situation is different for LSPs. Indeed, for a given surface S , one can define a plasmonic energy functional Ξ , which is the total surface charge-dipole interaction energy (see Supplementary Information), as:

$$\Xi = \frac{1}{4\pi} \oint_{S \times S} \frac{F^T + F}{2} ds ds' \quad (6)$$

The surfaces that respect $\delta\Xi|_S = 0$ are F -symmetric. Bi-orthogonality arises for surfaces for which $\delta\Xi|_S \neq 0$. While the time-reversal symmetry controls the hermiticity of parity-time-symmetric systems, the physical origin of the plasmonic bi-orthogonality is the violation of a variational principle.

Although singular, one can retrieve well-known features of other non-Hermitian systems in LSP physics, as summarized in Table 1. Indeed, as described in greater detail in the Supplementary Information, LSP modes are canonical examples of QNMs. Therefore, LSPs are analogous to parity-time-symmetric systems³⁸, which have been intensively investigated, particularly in optics^{39–42}. Moreover, the skewness of the vector space in LSP problems is measured by the overlap matrix, which is similar to the Petermann factor⁴ encountered in open quantum systems. The self-hybridization phenomenon investigated in this paper is a strong manifestation of the LSPs'

Table 1 | Table summing up the analogous quantities encountered in an open quantum system and a plasmonic system

Physical quantities	Open quantum cavity	Plasmonics
Time dependence	Dynamic	Static
Kernel	Non-Hermitian Hamiltonian H	Non-symmetric Coulomb kernel F
Eigenvalues	Complex energies ω_m	Real geometrical eigenvalues λ_m
Broken invariance	Time-reversal symmetry of H	F and S spatial symmetry
Constant characterizing the bi-orthogonality	Petermann factor K	Overlap matrix T_{nm}

bi-orthogonality. Several exotic effects arising in non-Hermitian systems such as power oscillations⁴³ or asymmetric propagation⁴⁰ of light in optical systems should therefore have a counterpart in LSPs. More generally, we expect all of the features of non-Hermitian systems to appear in LSP systems, particularly the presence of exceptional points.

Received: 10 July 2017; Accepted: 17 November 2017;

Published online: 01 January 2018

References

- Bender, C. M., Brody, D. C. & Jones, H. F. Complex extension of quantum mechanics. *Phys. Rev. Lett.* **89**, L391–L394 (2002).
- Heiss, W. D. The physics of exceptional points. *J. Phys. A* **45**, 444016 (2012).
- Brody, D. C. Biorthogonal quantum mechanics. *J. Phys. A* **47**, 035305 (2014).
- Lee, S. Y. Decaying and growing eigenmodes in open quantum systems: biorthogonality and the Petermann factor. *Phys. Rev. A* **80**, 1–9 (2009).
- Stehmann, T., Heiss, W. D. & Scholtz, F. G. Observation of exceptional points in electronic circuits. *J. Phys. A* **37**, 7813–7819 (2004).
- Lee, S.-Y. et al. Divergent Petermann factor of interacting resonances in a stadium-shaped microcavity. *Phys. Rev. A* **78**, 015805 (2008).
- Doppler, J. et al. Dynamically encircling an exceptional point for asymmetric mode switching. *Nature* **537**, 76–79 (2016).
- Shin, Y. et al. Observation of an exceptional point in a two-dimensional ultrasonic cavity of concentric circular shells. *Sci. Rep.* **6**, 38826 (2016).
- Leung, P. T., Liu, S. Y. & Young, K. Completeness and orthogonality of quasinormal modes in leaky optical cavities. *Phys. Rev. A* **49**, 3057–3067 (1994).
- Ching, E. S. C. et al. Quasinormal-mode expansion for waves in open systems. *Rev. Mod. Phys.* **70**, 1545–1554 (1998).
- Leung, P. T., Suen, W. M., Sun, C. P. & Young, K. Waves in open systems via a biorthogonal basis. *Phys. Rev. E* **57**, 6101–6104 (1998).
- Alaeian, H. & Dionne, J. A. Non-Hermitian nanophotonic and plasmonic waveguides. *Phys. Rev. B* **89**, 75136–75139 (2014).
- Heiss, W. D. Exceptional points: global and local aspects. *AIP Conf. Proc.* **597**, 311–318 (2001).
- Heiss, W. D. Mathematical physics: circling exceptional points. *Nat. Phys.* **12**, 823–824 (2016).
- Seyranian, A. P., Kirillov, O. N. & Mailybaev, A. A. Coupling of eigenvalues of complex matrices at diabolic and exceptional points. *J. Phys. A* **38**, 1723–1740 (2005).
- Kodigala, A., Lepetit, T. & Kanté, B. Exceptional points in three-dimensional plasmonic nanostructures. *Phys. Rev. B* **94**, 201103(R) (2016).
- Zheng, M. C., Christodoulides, D. N., Fleischmann, R. & Kottos, T. PT optical lattices and universality in beam dynamics. *Phys. Rev. A* **82**, 010103(R) (2010).
- Mayergoyz, I. D., Fredkin, D. R. & Zhang, Z. Electrostatic (plasmon) resonances in nanoparticles. *Phys. Rev. B* **72**, 155412 (2005).
- Ouyang, F. & Isaacson, M. Surface plasmon excitation of objects with arbitrary shape and dielectric constant. *Philos. Mag.* **60**, 481–492 (1989).
- Yin, X. & Zhang, X. Unidirectional light propagation at exceptional points. *Nat. Mater.* **12**, 175–177 (2013).
- Peng, B. et al. Parity time-symmetric whispering-gallery microcavities. *Nat. Phys.* **10**, 394–398 (2014).
- Hahn, C. et al. Observation of exceptional points in reconfigurable non-Hermitian vector-field holographic lattices. *Nat. Commun.* **7**, 12201 (2016).
- Choi, Y., Hahn, C., Yoon, J., Song, S. H. & Berini, P. Extremely broadband, on-chip optical nonreciprocity enabled by mimicking nonlinear anti-adiabatic quantum jumps near exceptional points. *Nat. Commun.* **8**, 14154 (2017).

- García de Abajo, F. & Aizpurua, J. Numerical simulation of electron energy loss near inhomogeneous dielectrics. *Phys. Rev. B* **56**, 15873–15884 (1997).
- Hohenester, U. & Trügler, A. MNPBEM – A Matlab toolbox for the simulation of plasmonic nanoparticles. *Comput. Phys. Commun.* **183**, 370–381 (2012).
- Bouadhar, G. & Kociak, M. Modal decompositions of the local electromagnetic density of states and spatially resolved electron energy loss probability in terms of geometric modes. *Phys. Rev. B* **85**, 245447 (2012).
- Fredkin, D. R. & Mayergoyz, I. D. Resonant behavior of dielectric objects (electrostatic resonances). *Phys. Rev. Lett.* **91**, 253902 (2003).
- Schmidt, F.-P. et al. Edge mode coupling within a plasmonic nanoparticle. *Nano. Lett.* **16**, 5152–5155 (2016).
- Das, P., Lourenço-Martins, H., Tizei, H. G. L., Weil, R. & Kociak, M. Nanocross: a highly tunable plasmonic system. *J. Phys. Chem. C* **121**, 16521–16527 (2017).
- Trügler, A., Tinguely, J.-C., Krenn, J. R., Hohenau, A. & Hohenester, U. Influence of surface roughness on the optical properties of plasmonic nanoparticles. *Phys. Rev. B* **83**, 81412 (2011).
- Schmidt, F.-P., Ditlbacher, H., Hofer, F., Krenn, J. R. & Hohenester, U. Morphing a plasmonic nanodisk into a nanotriangle. *Nano. Lett.* **14**, 4810–4815 (2014).
- Zener, C. Non-adiabatic crossing of energy levels. *Proc. Royal Soc. A* **137**, 696–702 (1932).
- Brown, L. V., Sobhani, H., Lassiter, J. B., Nordlander, P. & Halas, N. J. Heterodimers: plasmonic properties of mismatched nanoparticle pairs. *ACS Nano* **4**, 819–832 (2010).
- Novotny, L. Strong coupling, energy splitting, and level crossings: a classical perspective. *Am. J. Phys.* **78**, 1199–1202 (2010).
- Collins, S. M., Nicoletti, O., Rossouw, D., Ostasevicius, T. & Midgley, P. A. Excitation dependent Fano-like interference effects in plasmonic silver nanorods. *Phys. Rev. B* **90**, 155419 (2014).
- Nordlander, P., Oubre, C., Prodan, E., Li, K. & Stockman, M. I. Plasmon hybridization in nanoparticle dimers. *Nano. Lett.* **4**, 899–903 (2004).
- Nelayah, J. et al. Mapping surface plasmons on a single metallic nanoparticle. *Nat. Phys.* **3**, 348–353 (2007).
- Bender, C. M. & Boettcher, S. Real spectra in non-hermitian hamiltonians having PT-symmetry. *Phys. Rev. Lett.* **80**, 5243–5246 (1998).
- Guo, A. et al. Observation of PT-symmetry breaking in complex optical potentials. *Phys. Rev. Lett.* **103**, 093902 (2009).
- Rüter, C. E. et al. Observation of parity-time symmetry in optics. *Nat. Phys.* **6**, 192–195 (2010).
- Alaeian, H. & Dionne, J. A. Parity-time symmetric plasmonic metamaterials. *Phys. Rev. A* **89**, 033829 (2014).
- Muslimani, Z. H., Makris, K. G., El-Ganainy, R. & Christodoulides, D. N. Optical solitons in PT periodic potentials. *Phys. Rev. Lett.* **100**, 030402 (2008).
- Makris, K. G., El-Ganainy, R., Christodoulides, D. N. & Muslimani, Z. H. Beam dynamics in PT symmetric optical lattices. *Phys. Rev. Lett.* **100**, 103904 (2008).
- Gloter, A., Douiri, A., Tence, M. & Colliex, C. Improving energy resolution of EELS spectra: an alternative to the monochromator solution. *Ultramicroscopy* **96**, 385–400 (2003).

Acknowledgements

We thank O. Stéphan and M. Walls for in-depth reading of the manuscript. This work has received support from the French state managed by the National Agency for Research under the programme of future investment EQUIPEX TEMPOS-CHROMATEM with the reference ANR-10-EQPX-50.

Author contributions

P.D., H.L.-M. and M.K. designed the experiments. H.L.-M., P.D., L.H.G.T. and M.K. performed the EELS experiments. R.W., P.D. and H.L.-M. prepared the samples. H.L.-M., P.D. and L.H.G.T. analysed the data. H.L.-M. and M.K. performed the theoretical analysis. H.L.-M. performed simulations. H.L.-M. and M.K. wrote the manuscript. H.L.-M., P.D., L.H.G.T. and M.K. discussed experimental and theoretical results, and participated in improvement of the manuscript.

Competing interests

The authors declare no competing financial interests.

Additional information

Supplementary information is available for this paper at <https://doi.org/10.1038/s41567-017-0023-6>.

Reprints and permissions information is available at www.nature.com/reprints.

Correspondence and requests for materials should be addressed to M.K.

Publisher's note: Springer Nature remains neutral with regard to jurisdictional claims in published maps and institutional affiliations.

Methods

Sample preparation. We produced a series of silver nanodaggers with an increasing arm length by electron-beam lithography on 15-nm-thick Si_3N_4 substrates.

EELS spectral imaging. An EELS spectrum can be acquired by analysing the energy lost by a fast electron beam after interaction with a sample of interest. Electrons were generated in a scanning transmission electron microscope (STEM) and the EELS analyser consists essentially of a magnetic sector. A typical EELS spectrum for plasmonic particles consists of a peak at zero energy (the so-called zero-loss peak (ZLP)) containing all of the electrons not having interacted inelastically (within the system's energy resolution) with the sample. It is followed by a series of peaks at the plasmons energies. In modern STEMs, a nanometric electron beam can be scanned over the sample of interest, with one spectrum recorded at each scan step, resulting in a collection of spectra called a spectrum image. All of the experimental data presented in this paper have been extracted from such spectrum images. For each pixel, the electron intensity scattered to high angle (so called high angle annular dark field (HAADF) signal), which is roughly proportional to the mass under the electron beam, can be measured. At the end of the scan, an HAADF image can therefore be reconstructed and compared pixel-by-pixel with the spectra. All presented data were acquired with a VG HB-501 STEM except the spectrum image used to generate the fitted images in Fig. 3e,f, acquired on a NION USTEM200 (see Supplementary Information). Both STEMs are equipped with a cold field-emission gun operated at 60 or 100 kV and fitted with a home-made EELS detection system. The nominal energy resolution (full-width at half-maximum of the ZLP) was ≈ 300 meV. Beam sizes were typically 0.7 and 0.15 nm and spectrometer entrance apertures were typically of the same angular size as the incident beam.

EELS data treatment. EEL spectra were realigned spectrally. For further inspection, spectra were summed in regions of interest where particular modes

are dominant to increase signal-to-noise ratio. Maps of the modes can then be generated by filtering the spectra around the relevant energy. Without further treatment, the anti-crossing and mode distribution are already visible (see Supplementary Information). To further increase the precision of the peak position measurement (see energy diagram in Fig. 3), we performed EEL spectrum-image deconvolution using a Richardson–Lucy algorithm⁴⁴ with typically 25 iterations and resulting in a ZLP width of 0.15 eV. Spectra in Fig. 3, corresponding to the sum of typically 100–200 spectra each acquired over typically 0.1–0.5 ms, have been extracted from the corresponding region of interest. The high signal-to-noise ratio obtained allows for extremely high fit precision, with standard deviation typically smaller than 5 meV for the peak position (see Supplementary Information). In most cases, filtered maps could then be generated at energies corresponding to the different modes. In the case of strong coupling, however, the spectral overlap between two modes resulted in filtered images with mixed spatial features (see Supplementary Information). In this case, we generated fitted maps in which each pixel contains the (fitted) area under the given peak³⁷. This allowed us to unmix the spatial distributions of both modes. The full set of EELS maps is presented in the Supplementary Information.

Simulations. All of the simulations except Fig. 3b were carried out using the MNPBEM toolbox within the quasi-static formulation of the Maxwell equations and by considering only the first seven eigenmodes of each structure, as higher-order modes do not sensibly contribute to the spectra in the spectral range of interest of the paper. The simulations in Fig. 3b were performed using MNPBEM²⁵ in the retarded approximation, enabling a better accuracy in the mode energy positions with respect to the experiments.

Data availability. The data that support the plots within this paper and other findings of this study are available from the corresponding author upon reasonable request.